E-proceedings of the 36th IAHR World Congress
28 June – 3 July, 2015, The Hague, the Netherlands

Impulse waves generated by snow avalanches falling into lakes

GIANLUCA ZITTI(1), CHRISTOPHE ANCEY(2), MATTEO POSTACCHINI(1) & MAURIZIO BROCCHINI(1)

(1) Department of Civil and Building Engineering, and Architecture,
Polytechnic University of Marche, Via Brecce Bianche, 60131, Ancona, Italy,
g.zitti@univpm.it - m.postacchini@univpm.it - m.brocchini@univpm.it
(2) Faculté de l'Environnement Naturel, Architectural et Construit,
Ecole Polytechnique Fèdèrale de Lausanne, Lausanne, Switzerland
christophe.ancey@epfl.ch

ABSTRACT

In recent years, the number of water reservoirs in high-altitude areas has increased. They are often used to provide water for various activities related with recreational (i.e. skiing) and production activities. Many of such reservoirs are threatened by snow avalanches. To investigate the phenomenon, an experimental study was carried out at the Ecole Polytechnique Fédérale de Lausanne using a prismatic 3m-long flume. A mass of buoyant particles, initially at rest, was released into a water flume down a 30°-sloping ramp. Its impact with the water surface was analyzed in detail. During the tests, the impacting mass, the water depth in the flume and the ramp length were changed. Both the dynamics of the granular mass at the impact zone and the wave generation induced by the impact were acquired using a high-frequency camera and accurately analyzed. An analysis of the wave propagation along the flume, also captured by two lower-speed cameras, was made by mean of numerical analyses based on a depth-averaged Boussinesq-type model. A theoretical analysis has also been undertaken to assess how the sub-aerial mass dynamics influences energy dissipation, and to identify the key variables of the problem, i.e. the velocity at impact, the shape of the water volume displaced during the impact, the depth of the center of the submerged mass and the percentage of submerged mass.

Keywords: avalanche, tsunami, impulse waves

1. INTRODUCTION

The increasing anthropic pressure on high-altitude areas and sub-polar regions has fostered research on snow and avalanches. One of the recent problems of particular relevance to avalanche hazard assessment is the generation of tsunami-type waves due to the avalanche impact into a water basin, and the following propagation. The number of water reservoirs in high-altitude areas, including water resources for ski resorts, lakes for recreational activities, reservoirs for hydroelectricity production and water supply for artificial snow production in skiing areas, is increasing and many reservoirs are located in areas threatened by avalanches. Over the last decade, there have been numerous events of snow avalanches hitting water basins. For example, in March 2006, a reservoir for artificial snow production in Pelvoux (France) was filled by a high-speed, dry-snow avalanche. The mixture of water and snow led to the formation of a wet-snow avalanche, which swept through the forest and reached the crosscountry ski trails in the valley bottom. Further, in February 1999 an avalanche impacted a lake close to the village of Göschenen (Switzerland) and emptied it (Ammann, 1999). The resulting snow-water mixture flowed out as a thick viscous fluid and overtopped a 6-m protection wall, damaging the village structures and killing one person (Figure 1).

Figure 1. The village of Göschenen (Switzerland) in February 1999, after three avalanches, and the flow of a snow-water mixture (taken from Swiss Federal Topography Agency).

The avalanche-induced tsunami hazard is also high along the Northern Europe (Norway, Iceland) and Northern America (Alaska, Canada) coastline. Terrain (fjords with steep slopes) and climatic conditions (heavy precipitation and snow accumulation) are conducive to an intense avalanche activity. In the island of Stjernoya in the Altafjord, Northern Norway, the Lillebukt bay is often interested by avalanche sliding from the Nabbaren mountain (e.g., see Figure 2), so that triggered avalanches are being studied in this location (Frauenfelder et al. 2014). In October 1995, in Súðavík, Iceland, a 2-3 m-thick layer of compacted snow detached from an 800 m-wide channel at 500 m above the sea level, then extending for 200 m into the fjord and generating a 10 m-high wave that damaged several structures (Ágústsson and Sigurðsson, 2004).


a)
b)

Figure 2. Freeze frame taken from video footage of the April 8, 2014 avalanche. (Image credit: Sibelco Nordic - http://www.nrk.no/nordnytt/sprengtelos-enormt-snoskred-1.11658148)

Engineers are used to distinguishing between "flowing avalanches" (flow depth less than 10 m thick, density in the 150-500 kg/m^3 range, velocity ranging from 5 to 30 m/s) and particles suspended in air (10-100 m thick cloud, with mean density in the 5-50 kg/m^3 range and velocity in the 50-100 m/s range).

Avalanche formation and propagation course are closely related to meteorological conditions and terrain. The variability of the corresponding parameters explains why the avalanche dynamics is so complex. Statistical fluid-dynamics approaches have been developed for predicting the main features of avalanche motion and its maximum runout distance (Ancey, 2001, 2012). As field experiments are difficult to conduct and interpret, additional insights have been brought by small-scale laboratory experiments. Granular flows have been used to simulate flowing avalanches in the lab, while turbidity and density currents can reproduce the dynamics of powder airborne avalanches (Savage, 1989 and Hutter, 1996).

In the following section, small-scale experiments, exploiting the analogy between flowing avalanches and granular flows, are proposed for studying impulse waves generated by snow avalanches into water reservoirs. A two-dimensional physical model is used. The analysis of the main processes involved in the avalanche dynamics led to the selection of the following parameters: the granular mass, the water height and the slope length. In section 3, the experimental setup and protocol are reported, while section 4 summarizes the main results of the experimental campaign. The physical model proposed here shows similarities with that used in the studies on landslide-generated impulse waves (e.g., Fritz et al., 2003a, b). The main differences between avalanche impact and landslide impact are discussed. Correlations between the avalanche impulse and wave characteristics are obtained and compared with those pertaining to landslides. The motion of the submerged mass barycenter is also described. A preliminary attempt at numerically describing the wave propagation is reported in section 5. Some conclusions close the paper.

2. PHYSICAL MODEL

The physical model used to simulate an avalanche impact in water is a two-dimensional approximation of the problem. We consider a sloping ramp with inclination α, entering into a horizontal flume filled with still water. The still water depth is denoted by h (see section 3). The global coordinate system (x,y) is defined with the origin at the still water shoreline, the x-axis being positive streamwise and the y-axis downward. A further coordinate ξ, with the same origin, follows the ramp slope. A mass M, with initial density $\rho_m(0)$, is released at a distance l_s from the shoreline.

The granular material chosen to represent the avalanche mass is characterized by a grain diameter d_g and a density lower than that of the water $\rho_m(0)<\rho_w$. During the fall of the granular slide along the chute, the average density $\rho_m(t)$ and shape of the bulk vary with time as a result of volume expansion. The shape can be described by a function $s(\xi,t)$ representing the slide thickness at location ξ and time t. The mass shape at the impact corresponds to the value of the function at the shoreline $s(0,t)$. The velocity along the slope is described by the function $v_m(\xi,t)$. Since the granular mass density is lower than the water density, the bulk spreads into the water after the impact, initially sinking for a short time without reaching the flume bottom, then floating in the water. An index for the submerged mass motion is given by the position of the center of mass of the submerged grains $x_G(t),y_G(t)$.The impact on the water surface generates an impulse wave, described by the function $\eta(x,t)$. Figure 3 illustrates the two-dimensional physical model and the main problem parameters.

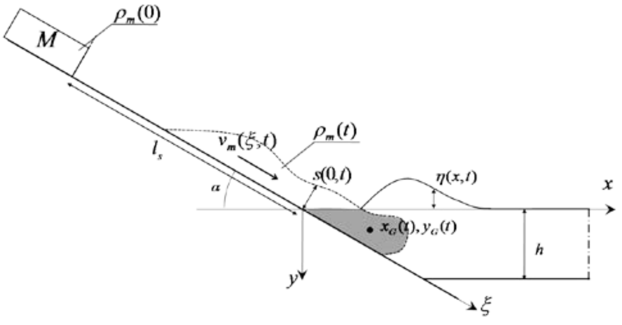

Figure 3. Two-dimensional physical model for an avalanche impacting into water. Both initial and impacting mass are illustrated. The submerged mass is identified by the shaded area.

The mass of the slide, M, and the gravitational acceleration, g, define the initial energy of the slide. They are two governing parameters for the dynamics. The slope length l_s can be neglected if we regard the problem as starting at the beginning of the impact. In that case the energy can be defined by the mass M and the slide impact velocity $v_m(0,t)$. The bulk density of the avalanche at the impact affects the momentum transfer to water, but is difficult to assess. It can be related to other parameters. First, we define the impact duration Δt as the time between the impact time of the first particle (t_{in}) and that of the last particle (t_{fin}), i.e. $\Delta t=t_{fin}-t_{in}$. Then, we define the mean avalanche thickness at the impact:

$$h_{m,in} = \frac{1}{\Delta t}\int_0^{\Delta t} s(0,t)dt \qquad [1]$$

and the length of the impacting slide $l_{m,in}$, related to the impact velocity, which is taken to be a constant (see section 3):

$$l_{m,in} = \Delta t \quad v_m(0,t) \qquad [2]$$

Finally, it is possible to define the avalanche volume:

$$V(t_{in}) = h_{m,in} \quad \Delta t \quad v_m(0,t) \quad b \qquad [3]$$

where b is the flow (flume) width. Now it is possible to express the impact density $\rho_m(t_{in})$ as a function of the mass M, the mean impact thickness $h_{m,in}$, the impact duration Δt and the impact velocity $v_m(0,t)$:

$$\rho_m(t_{in}) = \frac{M}{V(t_{in})} = \frac{M}{h_{m,in}\Delta t v_m(0,t) b} \qquad [4]$$

As b is fixed, while M and $v_m(0,t)$ are already included in the governing parameters, we can regard the mean avalanche thickness $h_{m,in}$ and the impact duration Δt as further governing parameters. In addition, the momentum transfer is also affected by the avalanche bulk density at rest $\rho_m(0)$, the slope angle α and the grain diameter d_g. The wave formation and propagation, also depend on the time t, the water density ρ_w, the water depth h and the wave propagation distance x.

Since the main phenomenon to be investigated is the propagation of surface water waves, Froude similarity is used. Fluid viscosity, surface tension, and elastic compression forces are taken to be negligible. In summary, we consider the following model parameters:

1. Mass M
2. Gravitational acceleration g
3. Slope length l_s
4. Slide impact velocity $v_m(0,t)$
5. Mean value of the slide impact shape $h_{m,in}$
6. Duration of the impact Δt
7. Slope angle α
8. Grains diameter d_g
9. Water depth h
10. Water density ρ_w
11. Avalanche bulk density at rest $\rho_m(0)$
12. Position x
13. Time t

Buckingham's theorem states that any further variable of the problem, e.g. the water elevation η, can be written as

$$\eta = \eta(M, g, l_s, v_m(0,t), h_{m,in}, \Delta t, \alpha, d_g, h, \rho_w, \rho_m(0), x, t) \qquad [5]$$

The involved dimensions are: length [L], mass [M] and time [T], thus three scaling parameters are chosen: gravitational acceleration g, water depth h and water density ρ_w. Hence, the following dimensionless (starred) parameters are defined:

1. Dimensionless slide mass $M^* = M/(\rho_w\ b\ h^2)$
2. Dimensionless slope length $l_s^* = l_s/h$
3. Slide Froude number $Fr= v_m/ (gh)^{0.5}$
4. Dimensionless average slide thickness $h^*_{m,in}= h_{m,in}/h$
5. Dimensionless duration of the impact $\Delta t^* = \Delta t\ (g/h)^{0.5}$
6. Slope angle α
7. Dimensionless grains diameter $d_g^*= d_g/h$
8. Dimensionless bulk density at rest $\rho^*_m(0)= \rho_m(0)/ \rho_w$
9. Dimensionless wave propagation distance $x^*=x/h$
10. Dimensionless time $t^*=t(g/h)^{0.5}$

The dimensionless form of [5] is:

$$\eta^* = \frac{\eta}{h} = \eta^*(M^*, l_s^*, Fr, h_{m,in}^*, \Delta t^*, \alpha, d_g^*, \rho_m^*(0), x^*, t^*) \qquad [6]$$

Seminal works on landslides modelled through block model experiments (Kamphuis and Bowering, 1972; Walder et al., 2003) suggest that the impact dimensionless volume and the Froude number are the key parameters. However, both impact volume and impact velocity are difficult to vary systematically and, therefore, other variables, from which they depend, are used here as governing parameters. The impact volume varies with the mass M and the average impact bulk density $\rho_m(t_{in})$, which also depends on $h_{m,in}$, Δt and $v_m(0,t)$. Since such variables are difficult to be controlled, we regard the bulk density at rest $\rho_m(0)$ and the slope length l_s as the controlling parameters, while $h_{m,in}$, Δt and $v_m(0,t)$ are measured. The impact velocity $v_m(0,t)$, taken as a governing parameter, indirectly varies by changing the slope length l_s.

In the present experiments, different Fr are obtained by varying the water depth h. The slope angle α, grain diameter d_g and bulk density at rest $\rho_m(0)$ are not varied.

3. EXPERIMENTAL CAMPAIGN

3.1 Experimental setting

The experimental setup is composed of a wooden chute, with slope angle α = 30°, reaching the bottom of a 3 m-long prismatic flume, with transparent glass sidewalls. Both chute and flume are 0.11 m wide. The flume is filled with water and three different water depths are used: h=0.11 m, 0.14 m and 0.18 m. The released mass M is composed of granular expanded clay, whose bulk density at rest $\rho_m(0)$ is about 500 kg/m^3, which is close to the compact snow density before of the avalanche detachment. The bulk density at rest $\rho_m(0)$ is measured for each mass release, before the experiment; its average over all the experiments is 489 kg/m^3, with a standard deviation of 8%. The average grain diameter is d_g=9 mm. For each value of h, the mass of the bulk is increased from 100 g to 700 g, by increments of 100 g. The mass is placed on the chute, at a distance l_s from the shoreline. Two lengths of the slide path are used, i.e. l_s=0.66 m and 1.21 m. The slide impact velocity $v_m(0,t)$, mean slide impact shape $h_{m,in}$ and impact duration Δt are measured using the equipment described in the following.

Three cameras are placed along the flume, with the optical axis perpendicular to the flume length. One is an high-speed camera, located in front of the shoreline, acquiring 256×785 px images at the impact zone, with a frequency of 1000 fps. A meshed metric grid is used to rectify the raw images and determine the size conversion factor. Two low-speed cameras are placed along the flume, collecting images with a resolution of 120×658 px and a frequency of 120 fps. The synchronized images of the two cameras are calibrated and merged using the meshed grid. A top view of the experimental setting is shown in Figure 4.

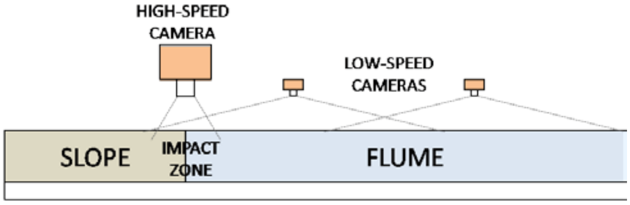

Figure 4. Sketch of the experimental setting.

Each experiment is repeated twice: both non-colored water (NCW), to better analyze the impact behavior of the slide, and colored water (CW), to study the wave formation and propagation, are used.

3.2 NCW Experiments

The NCW experiments have been designed to optimize the analysis of the dynamics of the submerged particles. For these experiments only the high-speed camera recording has been employed and images are used to estimate the controlling parameters $h_{m,in}$, Δt and $v_m(0,t)$, as well as the position of the center of mass of the submerged slide $x_G(t)$,$y_G(t)$.

The velocity $v_m(0,t)$ is evaluated using the high-speed camera images. The aerial part of the avalanche is studied and the image sequence is divided into 30 time intervals. For each interval the initial frame t_{sample} and another frame, with a delay of 0.003s with respect to t_{sample}, are analyzed. The two images are superposed giving a *sample*, shown in Figure 5, which is used to measure the displacement of the moving particles. The number of measurements for each sample depends on the quality of the image. Only samples containing a sufficient number of sliding particles are analyzed, hence the number of samples for each experiment is not the same, For each analyzed sample the mean value of the particle's displacement is evaluated and the impact velocity $v_m(0,t)$ is estimated, since the time delay is given. The measurement of the displacement has a precision of 0.45 mm (i.e. 0.5 px). The uncertainty on the velocity due to the measurement procedure is 0.15 m/s.

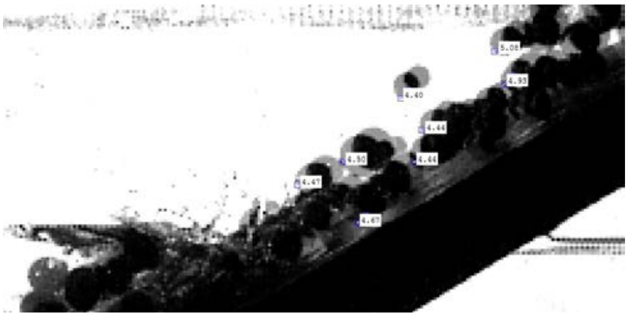

Figure 5. Sample used to evaluate particles displacement at the impact.

Table 1. Mean velocity and standard deviation of the mass at impact - for each experiment.

Exp ID	***n* [sample]**	**v_m [m/s]**	**σ_v [m/s]**
50	7	1.5896	0.1082
51	10	1.5214	0.1789
52	12	1.5074	0.1438
53	13	1.4837	0.0964
54	14	1.4340	0.1656
55	15	1.4381	0.1630
56	15	1.4418	0.2130
57	8	2.1819	0.1530
58	11	2.0521	0.1716
59	13	2.0247	0.2081
60	15	2.0331	0.1518
61	16	1.9143	0.1514
62	16	1.8538	0.1729
63	22	1.8064	0.2265
64	8	1.5508	0.1353
65	13	1.4957	0.1282
66	12	1.4240	0.1461
67	15	1.4689	0.1938
68	17	1.3942	0.2244
69	19	1.2404	0.2248
70	23	1.1124	0.2462
71	11	1.9420	0.1560
72	12	2.0240	0.3732
73	14	1.9303	0.2060
74	18	1.8009	0.1914
75	19	1.9450	0.1952
76	17	1.8179	0.2202
77	18	2.0115	0.1787
108	10	1.9749	0.1839
109	12	1.8671	0.1881
110	27	1.9164	0.1747
111	19	1.8410	0.2061
112	20	1.8409	0.1502
113	20	1.9434	0.1525
114	22	1.6964	0.1982
115	14	1.5866	0.1001
116	17	1.6227	0.1384
117	21	1.5241	0.1256
118	21	1.5282	0.1960
119	25	1.3727	0.1646
120	16	1.4116	0.1262
121	15	1.2424	0.2568

The obtained impact velocity $v_m(0,t)$ shows a consistent average value and a relatively small standard deviation (see Table 1), hence the impact velocity can be assumed to be constant over time and equal to the mean value of the sample velocities:

$$v_m(0,t) = v_m = mean(v_m(0,t_{sample})) \qquad [7]$$

Table 1 reports, for each experiment, the number of the samples used n, the mean velocity v_m and the standard deviation σ_V. From samples like the one shown in Figure 5 is evident that the velocity direction is parallel to the slope-ramp, then it can be projected as follows:

$$\vec{v}_m = v_m \vec{a} \quad with \quad \vec{a} = \begin{bmatrix} \cos\alpha \\ \sin\alpha \end{bmatrix} \qquad [8]$$

In order to evaluate $h_{m,in}$, Δt , $v_m(0,t)$ and $x_G(t)$, $y_G(t)$ from the video, each frame of each NCW video is treated using the procedure illustrated in Figure 6a-f. The analyzed frame (Figure 6b) is cropped, the contrast is increased and the grayscale image is converted into black and white, with a white cut value of 0.18, where 1 corresponds to white and 0 to black. This leads to images like the one reported in Figure 6d. The resulting sample is masked with an image (Figure 6c) obtained from the first frame, where no particles are in the water (Figure 6a), using the same image processing. The subtraction of the mask from the sample gives an image where only particles are represented (Figure 6e). Noisy pixels are then removed. In the final sample image (Figure 6f), particles appears as white pixels.

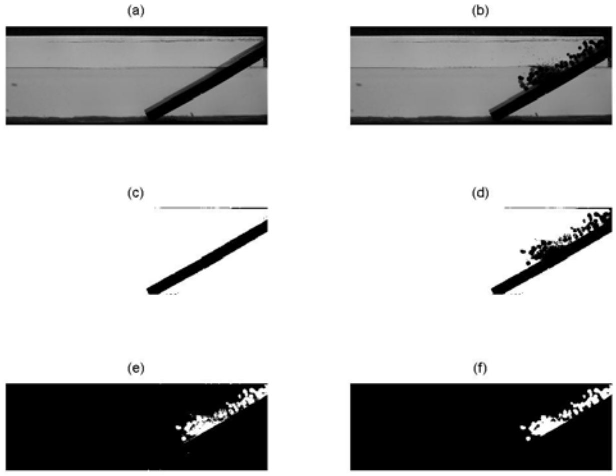

Figure 6 Example of processing of the video of the impact zone for the NCW experiments.

A similar procedure, with a larger white cut value, is used with the first image, to obtain a black-and-white image where the free surface at rest is captured. To evaluate $h_{m,in}$, a horizontal line (*level*) above the free surface is taken as reference, in order to avoid splashes and floating particles. The value of such *level* varies depending on the experiment, due to both the water depth and the intensity of the splashes. In practice it ranges from 15 mm to 40 mm. For each frame the horizontal slide thickness $s_h(level,t)$ is evaluated as the sum of the white pixels on the horizontal *level* in the final sample image. Then the thickness function is computed as the projection perpendicular to the slope: $s(0,t) = s_h(level,t)\sin\alpha$. The duration of the impact Δt is obtained from the estimate of both initial and final times of the impact. The former corresponds to the frame at which the first particle reaches the free surface, i.e. the first white pixel appears under the still water depth. The latter is more difficult to evaluate, because of splashes and floating particles, thus we assume that t_{fin} corresponds to the frame after which the shape function is lower than 5 pixels. The position $x_G(t)$, $y_G(t)$ of the center of mass of the submerged portion of the slide is evaluated as the barycenter of the area below the initial free surface.

3.3 CW Experiments

The CW experiments have been designed to optimize the reconstruction of the impulse wave generated by the slide impact. Both the high-frequency camera (at the impact zone) and the low-speed cameras (along the flume) are employed. Both sets of collected images are used to extrapolate the water elevation $\eta(x,t)$ of the generated impulse wave. Images from the high-speed camera are processed in order to obtain the main characteristics of the propagating wave, i.e. the maximum wave amplitude A_m, the maximum wave height H_m and the maximum wave period T_m. The spatial (x) and temporal (t) domains used for the analysis depend on the acquisition window, but also on the area affected by splashes and floating particles. Hence, for each experiment a proper space-time domain is chosen in order to have the maximum suitable area for a time lapse long enough to evaluate the maximum height and period. The water elevation at a fixed position can also be used as the boundary condition to initialize numerical simulations of the wave propagation.

Images coming from the two low-speed cameras are used both to estimate the wave energy and to benchmark the numerical simulations of the wave propagation.

Image processing is the same for both videos and a small sample is shown in Figure 7 Each frame is first cropped, to remove splashes and falling particles (Figure 7 a). The contrast is increased and the gray-scale image converted into a black-and-white image (Figure 7 b). From the resulting image, where the water is black, the free surface can be extracted. The difference between the obtained surface level and the still surface obtained from the first frame (Figure 7 c) gives the instantaneous water elevation $\eta(x,t)$ (Figure 7 d).

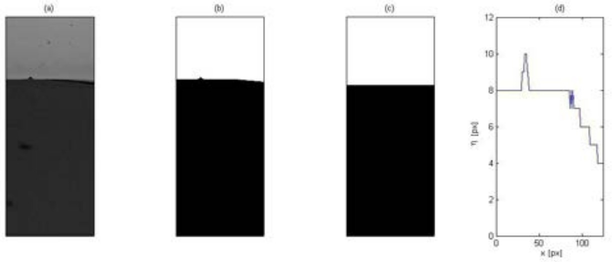

Figure 7 Sample of processing of the video of the wave propagation zone for CW experiment

The wave amplitude *A*, height *H* and period *T* are computed as functions of the position *x* and the time *t* within the cropped image. The maximum value of each property (A_m, H_m and T_m) and the corresponding locations (x_{Am}, x_{Hm} and x_{Tm}) are, thus, obtained.

4. RESULTS

4.1 Relations between avalanche and wave parameters

4.1.1 Dimensionless parameters

The dimensionless characteristics of the wave are the maximum dimensionless wave amplitude $A^*_m = A_m/h$, the maximum dimensionless wave height $H^*_m = H_m/h$ and the maximum wave period $T^*_m = T_m(g/h)^{0.5}$, with the corresponding dimensionless positions $x^*_{Am} = x_{Am}/h$, $x^*_{Hm} = x_{Hm}/h$ and $x^*_{Tm} = x_{Tm}/h$. All the stored dimesionless parameters are reported in Tables 2 and 3.

Table 2. Avalanche dimensionless parameters and wave dimensionless characteristics of experimental campaign – first part.

ID	50	51	52	53	54	55	56
M^*	0.047	0.093	0.139	0.186	0.232	0.279	0.325
I_s^*	4.714	4.714	4.714	4.714	4.714	4.714	4.714
Fr	1.356	1.298	1.286	1.266	1.224	1.227	1.230
$h^*_{m,in}$	0.094	0.118	0.132	0.148	0.167	0.152	0.171
Δt^*	0.054	0.080	0.099	0.117	0.113	0.126	0.134
A_m^*	0.041	0.059	0.067	0.070	0.077	0.099	0.086
x^*_{Am}	1.581	2.411	2.360	1.729	1.722	2.144	1.816
H_m^*	0.083	0.095	0.082	0.084	0.086	0.104	0.090
x^*_{Hm}	1.407	2.411	2.360	2.006	1.719	1.848	1.816
T_m^*	0.147	0.161	0.136	0.202	0.188	0.138	0.126
x^*_{Tm}	2.395	2.421	2.418	2.385	2.279	1.655	1.874
ID	**57**	**58**	**59**	**60**	**61**	**62**	**63**
M^*	0.046	0.093	0.138	0.186	0.231	0.278	0.318
I_s^*	8.643	8.643	8.643	8.643	8.643	8.643	8.643
Fr	1.862	1.751	1.728	1.735	1.633	1.582	1.541
$h^*_{m,in}$	0.082	0.108	0.107	0.112	0.133	0.145	0.127
Δt^*	0.059	0.087	0.113	0.137	0.129	0.142	0.184
A_m^*	0.038	0.054	0.061	0.070	0.078	0.075	0.079
x^*_{Am}	1.191	1.658	1.742	2.379	2.092	1.948	2.208
H_m^*	0.087	0.108	0.097	0.114	0.082	0.091	0.084
x^*_{Hm}	1.552	1.841	1.713	2.025	2.092	2.459	2.257
T_m^*	0.126	0.145	0.158	0.196	0.141	0.190	0.214
x^*_{Tm}	1.140	1.931	2.289	2.363	2.173	2.450	2.208
ID	**64**	**65**	**66**	**67**	**68**	**69**	**70**
M^*	0.028	0.055	0.084	0.112	0.139	0.168	0.193
I_s^*	3.667	3.667	3.667	3.667	3.667	3.667	3.667
Fr	1.167	1.126	1.072	1.105	1.049	0.933	0.837
$h^*_{m,in}$	0.038	0.042	0.059	0.056	0.064	0.081	0.069
Δt^*	0.073	0.122	0.114	0.162	0.155	0.182	0.291
A_m^*	0.020	0.051	0.051	0.046	0.055	0.051	0.066
x^*_{Am}	2.321	1.307	1.490	3.356	2.361	3.108	1.490
H_m^*	0.045	0.066	0.065	0.061	0.060	0.057	0.071
x^*_{Hm}	2.321	1.787	1.856	1.693	2.361	2.712	2.623
T_m^*	0.190	0.208	0.202	0.208	0.182	0.187	0.197
x^*_{Tm}	3.257	3.306	2.024	2.079	2.391	2.742	3.014

Table 3. Avalanche dimensionless parameters and wave dimensionless characteristics of experimental campaign – second part.

ID	71	72	73	74	75	76	77
M^*	0.028	0.056	0.084	0.112	0.136	0.168	0.195
I_s^*	6.722	6.722	6.722	6.722	6.722	6.722	6.722
Fr	1.461	1.523	1.453	1.355	1.464	1.368	1.514
$h^*_{m,in}$	0.026	0.041	0.045	0.055	0.053	0.063	0.072
Δt^*	0.113	0.111	0.149	0.168	0.197	0.181	0.194
A_m^*	0.024	0.036	0.059	0.050	0.056	0.050	0.062
x^*_{Am}	3.618	2.519	1.351	2.371	2.227	2.198	2.000
H_m^*	0.049	0.075	0.082	0.072	0.062	0.060	0.067
x^*_{Hm}	3.618	2.534	1.693	1.915	2.564	2.198	2.000
T_m^*	0.179	0.198	0.213	0.229	0.211	0.200	0.198
x^*_{Tm}	3.227	2.227	2.668	2.782	3.598	3.133	3.014
ID	**108**	**109**	**110**	**111**	**112**	**113**	**114**
M^*	0.076	0.150	0.223	0.298	0.376	0.450	0.526
I_s^*	11.00	11.00	11.00	11.00	11.00	11.00	11.00
Fr	1.901	1.797	1.845	1.772	1.772	1.871	1.633
$h^*_{m,in}$	0.081	0.119	0.121	0.112	0.178	0.107	0.162
Δt^*	0.062	0.081	0.110	0.157	0.131	0.257	0.220
A_m^*	0.051	0.067	0.066	0.083	0.098	0.106	0.117
x^*_{Am}	3.021	3.329	4.608	4.390	4.454	4.705	3.272
H_m^*	0.110	0.133	0.145	0.124	0.108	0.131	0.125
x^*_{Hm}	3.021	3.094	4.041	4.049	4.463	4.390	4.284
T_m^*	0.159	0.179	0.184	0.177	0.188	0.180	0.169
x^*_{Tm}	4.535	4.535	4.584	4.260	4.738	4.714	3.296
ID	**115**	**116**	**117**	**118**	**119**	**120**	**121**
M^*	0.076	0.144	0.226	0.300	0.372	0.442	0.527
I_s^*	6.00	6.00	6.00	6.00	6.00	6.00	6.00
Fr	1.527	1.562	1.467	1.471	1.321	1.359	1.196
$h^*_{m,in}$	0.085	0.126	0.132	0.129	0.169	0.211	0.306
Δt^*	0.074	0.085	0.141	0.166	0.175	0.165	0.230
A_m^*	0.049	0.060	0.082	0.089	0.110	0.106	0.118
x^*_{Am}	2.251	2.438	2.446	4.705	3.102	3.669	3.142
H_m^*	0.107	0.101	0.104	0.107	0.116	0.123	0.122
x^*_{Hm}	2.251	2.567	4.130	3.896	3.904	3.628	4.001
T_m^*	0.155	0.136	0.193	0.160	0.139	0.144	0.166
x^*_{Tm}	4.163	3.847	4.406	3.142	2.535	3.815	3.863

4.1.2 Comparison with landslide models

A physical model similar to that presented here has been used in studies of landslide-generated impulse waves (Fritz et al., 2003a; Fritz et al., 2003b; Fritz et al., 2004).

Some important differences make the present model more suited to describe the dynamics induced by snow avalanches. First the bulk density of the mass at rest for a landslide is always relatively large, i.e. $\rho_{m,la}(0)$>700kg/m^3, while for an avalanche it is significantly smaller, i.e. $\rho_{m,av}(0)$<500kg/m^3. Furthermore, in typical landslide models the granular slide is controlled by a piston: in this manner most parameters are more easily varied in a systematic way but it is hardly possible to promote a dilution of the bulk, as seen for avalanches. Our experimental setup differs from Fritz's setup because the motion of the granular mass is only due to the gravitational field: this makes some parameters more difficult to be controlled, but a large volume expansion is allowed for, as in real-life avalanches. Moreover, the large impact density and mass of landslides induce a clear phase separation and the bulk reaches the bottom of the flume, while in the present granular-avalanche model the material is dispersed and, because of its lower density, particles first sink (never reaching the bottom) and then float in the water, as evident in Figure 8.

The parameters varied in landslide models are the dimensionless mass M^*, the dimensionless mean thickness $h^*_{m,in}$, the Froude number Fr and the slope angle α, while the measured variables are the dimensionless duration of the underwater motion t^*_s and the slide dimensionless length at impact $l^*_{m.in}$. In contrast, in the present model, the varied (i.e. governing) parameters are the dimensionless mass M^* and the dimensionless slope length l^*_s, which influence the measured variables $h^*_{m,in}$, Fr, Δt^* and $l^*_{m.in}$. The impact dimensionless duration Δt^*, which is a fundamental variable in the present model, is neglected in landslide models.

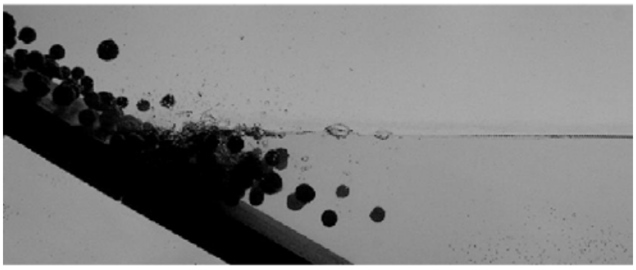

Figure 8. Example of floating particles and dispersion of particles in the water.

For landslide-generated impulse waves relations between wave and landslides characteristics are parameterized to be based on an impulse product parameter P (Heller et al., 2010), which is related to the square root of the streamwise slide momentum flux component (Zweifel et al., 2006). Such a parameter is built with M^*, $h^*_{m,in}$, Fr and $\cos(\alpha)$ and its actual definition is based on use of the available experimental data.

4.1.3 Impulse product parameter

We evaluate the momentum flux of an avalanche as follows: we consider that an avalanche of duration Δt and mass M has a mass flow rate given by:

$$Q_m = \frac{M}{\Delta t} \qquad [9]$$

Since the velocity of the avalanche is found to be constant in the experiments, the momentum flux is:

$$\vec{Q} = \frac{M \quad \vec{v}_m}{\Delta t} \qquad [10]$$

Thus, it is possible to define an impulse product parameter for an avalanche in terms of the dimensionless duration of the impact Δt^*, instead of the dimensionless mean thickness $h^*_{m,in}$. In fact the two parameters are connected through Eq [1]. Then, two different impulse product parameters are proposed for avalanches: the first one involves the dimensionless duration of the impact Δt^*:

$$P_{\Delta t} = Fr^{e_F} M^{*e_M} \Delta t^{*e_T} \cos\alpha^{e_\alpha} \qquad [11]$$

and the second one involves the dimensionless mean thickness $h^*_{m,in}$:

$$P_h = Fr^{e_F} M^{*e_M} h^{*e_h}_{m,in} \cos\alpha^{e_\alpha} \qquad [12]$$

The exponents e_F, e_M, e_t, e_α and e_h are evaluated as the coefficients that give the best fitting predictions for variables of interest, e.g. A^*_m, through relations:

$$A^*_m = kP^{e_P} \qquad [13]$$

where the coefficient k and the exponent e_P are themselves evaluated, through a nonlinear regression, as the values which best fit the dimensionless wave amplitude. In order to fit the dimensionless maximum wave amplitude A^*_m we vary the exponents and coefficients in the [0:1] range except for e_t, which is varied in the [-1:0] range, since it is reciprocal of the momentum flux in Eq. [10]. The best fit for A^*_m with $P_{\Delta t}$ is

$$A^*_m = 0.5P_{\Delta t} \quad with \quad P_{\Delta t} = Fr^{0.2} M^{*0.8} \Delta t^{*-0.2} \cos\alpha^{0.7} \qquad [14]$$

which gives a coefficient of determination R^2=0.88. Further the best fit for A^*_m with P_h is

$$A^*_m = 0.2P_h^{0.5} \quad with \quad P_h = Fr^{0.4} M^{*0.9} h^{*e_h 0.3}_{m,in} \cos\alpha^{0.7} \qquad [15]$$

which gives a coefficient of determination R^2=0.90. Comparison between empirical trends and experimental data are illustrated, respectively, in Figure 9 (A^*_m vs $P_{\Delta t}$) and Figure 10 (A^*_m vs P_h). The two impulse product parameters in Eqs. [14] and [15] are similar: in both cases the dimensionless mass is the most significant controlling variable, Δt^* and $h^*_{m,in}$ display an exponents of opposite sign, as expected from Eq. [1], while Fr is of lesser influence. However, the dependence of A^*_m on Fr differs in Eqs. [14] and [15]. A similar analysis is ongoing to derive predictive relations for both the maximum dimensionless wave height H^*_m and the maximum wave period T^*_m.

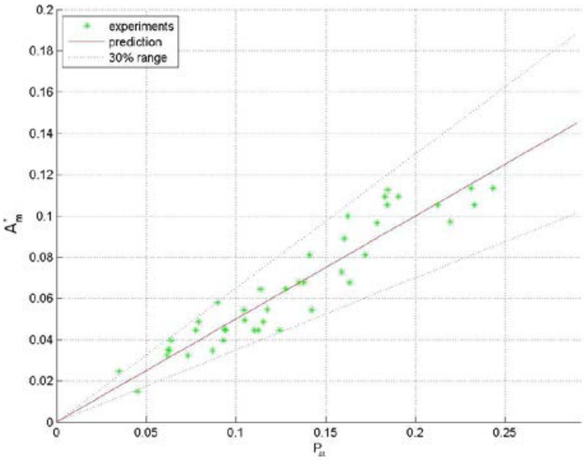

Figure 9. Comparison of the predictive relation $A^*_m=0.5P_{\Delta t}$ with experimental values.

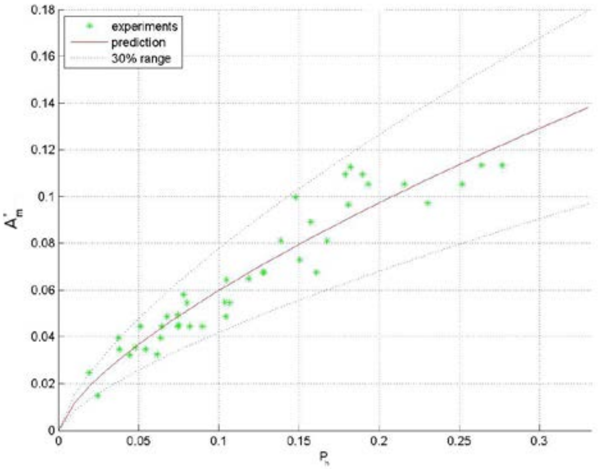

Figure 10. Comparison of predictive relation $A^*_m=0.2P_h^{0,5}$ with experimental values.

4.2 Avalanche and wave energies

The amplitude $\eta(x,t)$, extrapolated from the low-speed cameras along the entire flume length, is used to evaluate the energy of the wave propagating in the flume. The wave potential energy is computed as:

$$E_{w,pot}(t)=\frac{1}{2}\rho_w g b\int_{x_o}^{x_{end}}\eta(x,t)^2\,dx \qquad [16]$$

where the integration domain goes from the limit of the splash zone (x_o) to the end of the flume (x_{end}). In order to estimate the kinetic wave energy, the horizontal depth-averaged velocity $u(x,t)$, not available from the measurements, is reconstructed using the shallow water solution, i.e. the numerically-reconstructed velocity for the available experimental water surface elevation, and the wave kinetic energy is evaluated as:

$$E_{w,kin}(t)=\frac{1}{2}\rho_w b\int_{x_o}^{x_{end}}u(x,t)^2\,dx \qquad [17]$$

These energies are compared with the energy of the avalanche at impact. Given our choice for the coordinate system, the avalanche's energy at impact includes the kinetic energy contribution only:

$$E_{s,kin}=\frac{1}{2}Mv_m^2 \qquad [18]$$

The energy transfer is evaluated as the ratio between the maximum value of the wave energy and the energy of the avalanche at impact. The ratio results in the following range:

$$0.02\le\frac{\max\left(E_{w,pot}(t)+E_{w,kin}(t)\right)}{E_{s,kin}}\le 0.48 \qquad [19]$$

which is in line with the results found in the literature for landslides (e.g. Huber, 1980; Fritz et al. 2004).

4.3 Submerged mass barycenter motion

Inspection of the relative barycenter depth $y^*_G(t^*)$ suggested us to split the experiments into two groups: the first group includes experiments with relatively small masses, M=100÷200 g, while the second group corresponds to larger masses, M=400÷700 g.

For the first group the horizontal position of the submerged mass barycenter in time, $x^*_G(t^*)$, is parabolic during the initial stages of the impact and linear in the rest of the evolution (Figure 11), while the time variation of the vertical position, $y^*_G(t^*)$, is closely approximated by a parabola at short times, then by an hyperbola at longer times (Figure 12). For cases belonging to the second group the horizontal position of the submerged mass barycenter, $x^*_G(t^*)$, displays a linear time dependence, but the rate differs between short and long times (Figure 13). The depth curve, $y^*_G(t^*)$, is closer to a parabola during the first stage and linear in the following one (Figure 14).

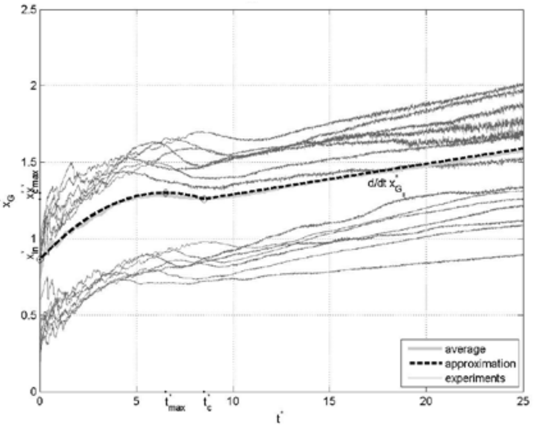

Figure 11. Horizontal motion of the submerged mass barycenter for experiments with M=100÷200g.

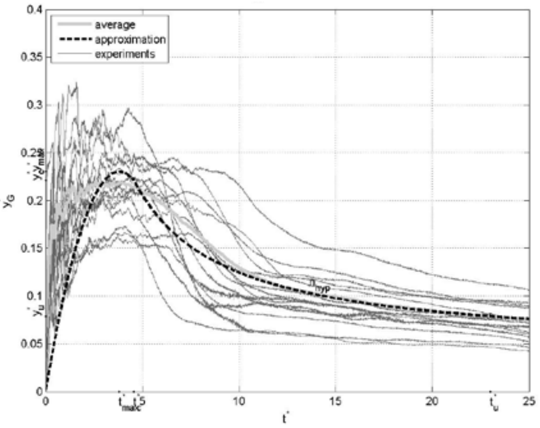

Figure 12. Vertical motion of the submerged mass barycenter for experiments with M=100÷200g.

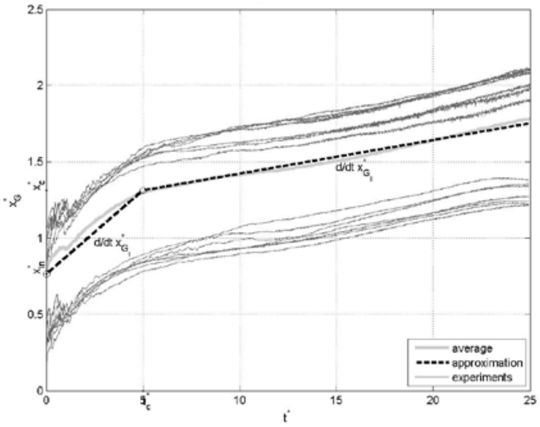

Figure 13. Horizontal motion of the submerged mass barycenter for experiments with M=400÷700g.

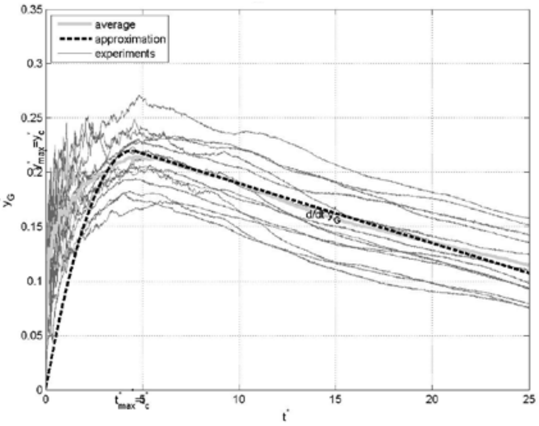

Figure 14. Vertical motion of the submerged mass barycenter for experiments with M=400÷700g.

The approximate functions of $x^*_G(t^*)$ and $y^*_G(t^*)$ for the two groups are related to control parameters which depend on the experimental data. An example of the approximate functions of each group is shown in Figure 11, Figure 12, Figure 13 and Figure 14, where the mean (ensemble) value of each group's experimental data is fitted.

These approximate functions are fairly complicated. For example, for the first group the following approximating functions can be used:

$$x^*_G(t^*) = \begin{cases} At^{*2} + Bt^* + x^*_{in} & for \quad t^* \le t^*_c \\ x^*_c + x^*_{II}(t^* - t^*_c) & for \quad t^* \ge t^*_c \end{cases} \qquad [20]$$

with

$$A = \frac{x^*_{in} - x^*_{\max}}{t^{*2}_{\max}} \quad B = -2Ax^*_{\max} \quad x^*_c = x^*_G(t^*_c) \qquad [21]$$

and

$$y^*_G(t^*) = y\begin{cases} At^{*2} + Bt^* & for \quad t^* \le t^*_c \\ y^*_c + C(t^{*n_{hyp}} - t_c^{*n_{hyp}}) & for \quad t^* \ge t^*_c \end{cases} \qquad [22]$$

with

$$A = -\frac{y^*_{\max}}{t^{*2}_{\max}} \quad B = -2Ay^*_{\max} \quad C = \frac{y^*_u - y^*_c}{t_u^{*n_{hyp}} - t_c^{*n_{hyp}}} \quad y^*_c = y^*(t^*_c) \qquad [23]$$

where x^*_{in} is the dimensionless initial distance from the shoreline, x^*_{max} is the dimensionless maximum distance from the shoreline in the parabolic part, t^*_{max} is the dimensionless time when x^*_{max} occurs, t^*_c is the matching dimensionless time, x^*_{II} is the slope of the linear part, y^*_{max} is the dimensionless maximum depth reached by the barycenter, t^*_{max} is the dimensionless time when y^*_{max} occurs, y^*_u is the dimensionless longterm depth (evaluated for t^*_u=23) and n_{hyp} is the exponent of the hyperbolic part.

Regressions lead to a fairly good fit for the first group (small masses), with R^2≥0.75, and very good fit for the second group (large masses), with R^2≥0.90. The regression ranges are reported in Table 4 and an example (experiment 50) of the fit for $x^*_G(t^*)$ and $y^*_G(t^*)$ is shown in Figure 15 and Figure 16.

Table 4. Range of variation for the parameters of the approximate function for the first group of experiments

Function parameter	Regression range
x^*_{in}	$0.2 < x^*_{in} < 1.3$
x^*_{max}	$x^*_{in} < x^*_{max} < 1.7$
t^*_{max}	$3 < t^*_{max} < 10$
t^*_c	$t^*_{max} < t^*_c < min(2.5^*\ t^*_{max}, 12)$
$\dot{x}^*_{II}$	$0.005 < \dot{x}^*_{II} < 0.1$
y^*_{max}	$0.15 < y^*_{max} < 0.35$
t^*_{max}	$1 < t^*_{max} < 8$
t^*_c	$t^*_{max} < t^*_c < 1.5t^*_{max}$
y^*_u	$0 < y^*_u < 0.15$
n_{hyp}	$-1 < n_{hyp} < 0.1$

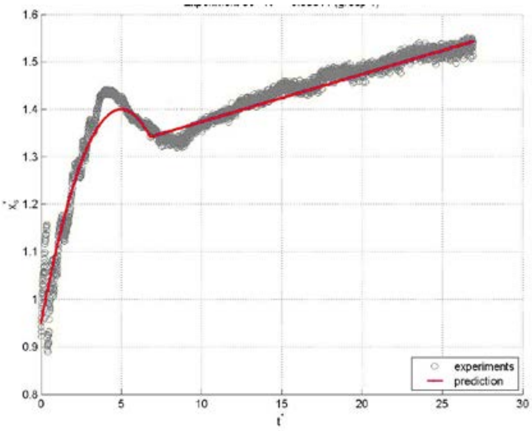

Figure 15. Approximate function for $x^*_G(t^*)$ for experiment 50 (small mass group), which gives R^2=0.95.

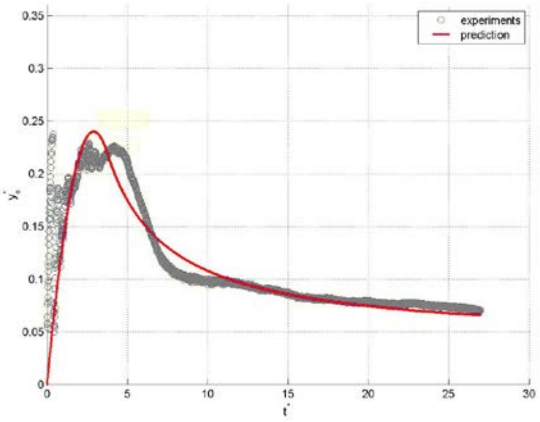

Figure 16. Approximate function for $y^*_G(t^*)$ for experiment 50 (small mass group), which gives R^2=0.81.

5. NUMERICAL SIMULATIONS

To better understand the physics of the phenomenon under investigation, the propagation of the impulse wave throughout the flume is studied. Such an analysis is undertaken by means of a Boussinesq-type numerical solver commonly used for shallow water applications, hence characterized by depth-averaged quantities (Shi et al., 2012). The equations chosen for the impulse wave propagation are fully nonlinear. The water surface level, which is first extracted from the data collected by the high-speed camera (as explained in section 3.3), is then decomposed in all its wave components using a Fast Fourier Transform. These are used to generate the periodic boundary condition for the numerical model (for details, see Wei et al., 1999). The other boundaries are reflective, representing the flume lateral and end walls. The numerical domain, of dimensions equal to those of the experimental flume (see section 3.1), is discretized by a (Δx, Δy)=(2, 2) cm grid.

However, modeling is difficult because the generated wave is characterized by a three-dimensional evolution, due to the particle dispersion both in the horizontal plane and along the vertical. The result is that the depth-averaged velocity and phase speed of the wave are not well captured by the model, the numerical wave being reproduced with some delay, and the wave shape being not very accurate. An example of the results is illustrated in Figure 17, where the numerical results are compared with the corresponding original and filtered experimental data.

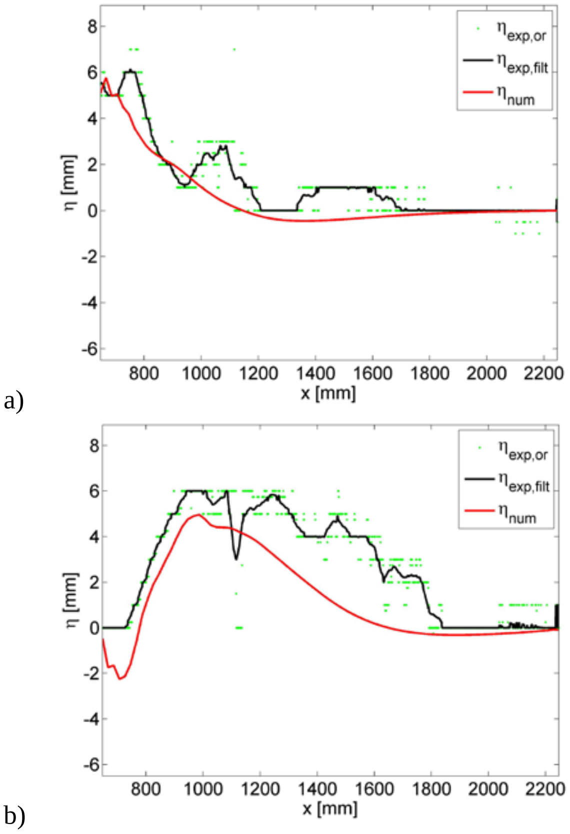

Figure 17. Comparison between numerical results (—) and experimental original (•) and filtered (—) data at 0.74 s (a) and 1.11 s (b).

6. CONCLUSIONS

A simple experimental setup, for a two dimensional physical model, is used to simulate the impact of snow avalanches in water, the motion of the submerged mass, the wave formation and the wave propagation.

A relation between the avalanche dimensionless parameters and the dimensionless maximum wave amplitude A^*_m is sought by introducing the impulse product parameter, inspired by a similar parameter used for describing landslide-induced impulse waves. The relation between Δt^* and $h^*_{m,in}$ suggests the possibility of using *the former* instead of *the latter* in the definition of an impulse product parameter suitable for avalanches. In fact in the two proposed impulse product parameters of Eqs. [14] and [15] Δt^* and $h^*_{m,in}$ have a similar importance, with an exponent of opposite sign. The possible use of the impact duration instead of the impact thickness in a predictive relation could be useful in view of the difficulties in evaluating the avalanche thickness at the impact.

Results on energy transfer is in line with literature results on landslide generated impulse wave. This endorses the validity of applying concepts typical of studies on landslide-induced impulse waves to the analysis of avalanche-induced waves.

The analysis of the motion of the submerged mass barycenter revealed two different behaviors depending on the slide mass. Such behavior can be described through polynomial and exponential functions, but the piecewise nature of these functions makes the finding of a relation between the coefficients of the approximating function and the avalanche's dimensionless parameters rather difficult. However, we are currently looking for a simpler approximation for the vertical motion of the submerged mass barycenter in similarity to that of a damped harmonic oscillator. Improved numerical simulations of the impulse waves are also ongoing.

ACKNOWLEDGMENTS

The experimental campaigns at the basis of the present work have been carried out during research visits of Maurizio Brocchini and Gianluca Zitti at the LHE-EPFL.

REFERENCES

Ágústsson K. and Sigurðsson HÞ., (2004), Hættumat fyrir Suðureyri í Súgandafirði. *Report 04023, Icelandic Meteorological Office*, 16.

Ammann WJ. (1999) *Der Lawinenwinter*, Eidgenössisches Institut für Schnee- und Lawinenforschung, Davos. pp. 588,

Ancey C., (2001). Snow Avalanches. *Geomorphological Fluid Mechanics, Lecture Notes in Physics*, 582, 319-338

Ancey C., (2012). Gravity Flow on Steep Slope, in *Buoyancy Driven Flows*, edited by E. Chassignet, C. Cenedese, and J. Verron. Cambridge University Press, New York, 372-432,

Frauenfelder R., Jònsson A., Lied K., Schwerdtfeger d., Bergum G., Buhler Y., Stoffel L. (2014), Analysis of an artificially triggered avalanche at the Nepheline Syenite Mine on Stjernøya, Alta, Northern Norway. *Proc International Snow Science Workshop 2014 Proceedings, Banff, Canada*

Fritz HM., Hager WH. and Minor HE. (2003). Landslide generated impulse waves. 1. Instantaneous flow fields. *Experiments in Fluids*, 35, 505-519

Fritz HM., Hager WH. and Minor HE (2003). Landslide generated impulse waves. 2. Hydrodynamic impact craters". *Experiments in Fluids*, 35, 520-532.

Fritz HM., Hager WH. and Minor, HE. (2004). Near field characteristics of landslide generated impulse waves. *Journal of Waterway, Port, Coastal, and Ocean Engineering*, 130(6), 287-302

Heller V. and Hager WH. (2010). Impulse product parameter in landslide generated impulse waves. *Journal of Waterway, Port, Coastal, and Ocean Engineering*, 136(3), 145-155

Huber, A. (1980). Schwallwellen in *Seen als Folge von Bergstürzen*. VAW-Mitteilung, D. Vischer, ed., Vol. 47, Versuchsanstalt für Wasserbau, Hydrologie und Glaziologie, ETH, Zürich, Switzerland, (in German).

Hutter K. (1996) Avalanche dynamics, in Hydrology of Disasters, *edited by V.P. Singh. Kluwer Academic Publications,* Dordrecht, 317-392.

Kamphuis, JW., and Bowering, RJ. (1972). Impulse waves generated by landslides. *Proc., 12th Coastal Engineering Conf.*, 1, ASCE, New York, 575–588.

Savage SB.,(1989) Flow of granular materials, in *Theoretical and Applied Mechanics*, edited by P. Germain, J.-M. Piau, and D. Caillerie. Elsevier, Amsterdam, 241-266.

Shi F., Kirby JT., Harris JC., Geiman JD., and Grilli ST. (2012). A high-order adaptive time-stepping TVD solver for Boussinesqe modeling of breaking waves and coastal inundation. *Ocean Modeling*, 43-44, 36-51

Walder, J.S., P. Watts, O.E. Sorensen, and K. Janssen (2003). Tsunamis generated by subaerial mass flows, *J. Geophys. Res.*, 108(B5), 2236(2).

Wei G., Kirby J.T., Sinha A. (1999). Generation of waves in Boussinesq models using a source function method. *Coastal Engineering*, 36, 271-299.

Zweifel A., Hager WH. And Minor HE. (2006). Plane impulse waves in reservoirs. *Journal of Waterway, Port, Coastal, and Ocean Engineering*, 132(5), 358-368